Letters

Quantum Power Pulse Combination Modulation to Achieve Full Load Range ZVS of DAB Converters in Wide Voltage Gain

Zhihua Fan, Haifeng Lu, *Senior Member, IEEE*, Jianyun Chai, and Xudong Sun

***Abstract*—Zero voltage switching (ZVS) is of great importance for reducing the switching loss in the dual active bridge (DAB) converter. Traditional phase-shift control for DAB is affected by the junction capacitance of switches, leading to an inherent non-ZVS region. This letter proposes a quantum power pulse combination modulation to fill the non-ZVS gap, which regulates power through a sequence of power or nonpower pulses with integer periods. During nonpower periods, one bridge generates a zero level voltage, thus the inductor current can behave as a controllable magnetizing current by adjusting the duty cycle of the other bridge, allowing seamless transitions between the two adjacent periods. The proposed method makes DAB operate at intermittent continuous-current mode, and realize ZVS in the region of light load and wide voltage gain, especially near unity gain. As the load increases beyond a certain power, the nonpower pulses disappear naturally, and the method reverts to traditional control. Experiment results confirm that the efficiency of the DAB is significantly improved, and no dc offset occurs in the inductor current.**

***Index Terms*—Continuous-current mode (CCM), dual active bridge (DAB), intermittent mode, quantum power pulse combination (QPPC), zero voltage switching (ZVS).**

I. Introduction

THE soft switching characteristics for all switches in the dual active bridge (DAB) play a vital role in reducing the switching loss and improving the efficiency. Due to the impact of junction capacitance, conventional triple phase-shift (TPS) control [1], [2], [3] with multimode modulation for DAB inherently results in a nonzero voltage switching (ZVS) region. To achieve soft switching in full load range, the triangular modulation (TRM) [4], [5] operates the inductor current in discontinuous conduction mode (DCM), facilitating zero-current switching (ZCS) in the non-ZVS region, but this comes at the cost of losing ZVS, resulting in some efficiency loss. The trapezoidal modulation (TZM) [6] injects reactive current to improve the ZVS at light load by redesigning the magnetizing inductance. However, due to the uncontrollable nature of the magnetizing current, a larger magnetizing current is required to achieve ZVS, which increases conduction losses. Moreover, the magnetizing current can only be injected into a single bridge.

A more efficient method to fill the non-ZVS gap is the time-sharing mixed-mode modulation [7], which operates alternatively between two ZVS-enabled modes for heavy and light loads. To ensure smooth transitions between different modes, some additional adjustable periods are inserted. An obstacle to mixed-mode modulation is the absence of a ZVS region near the corner of the unity voltage ratio and light load [1]. The intermittent continuous-current mode (CCM) modulation [8] mixes normal power ZVS intervals with nonpower intervals, during which both the primary and secondary bridges are forced to zero level, allowing the residual current to circulate naturally through each bridge. The circulating current assists the switches in performing ZVS, but its unidirectional flow leads to a significant dc bias in the inductor current, which negatively impacts ZVS. Extra phase-shift compensation is required to ensure a smooth current transition. Furthermore, this method only addresses the case where the voltage ratio is equal to unity.

To fill the non-ZVS gap, this letter proposes the quantum power pulse combination (QPPC) modulation, which regulates power through a sequence of integer power or nonpower pulses with a fixed period.

The rest of this letter is organized as follows. Section II illustrates the working principle of QPPC. In Section III, experimental results are given as verification. Finally, Section IV concludes this letter.

II. Novel Modulation Method

The circuit diagram of a DAB converter is shown in Fig. 1. M is defined as $V_2/(nV_1)$. This letter takes forward power flow and $M < 1$ as an example to illustrate the operating principle.

In [9], due to the influence of switch junction capacitance and dead time, the ZVS region of mode A under traditional phase-shift control has a lower power boundary (P_{A_cri}), while that of mode B has an upper power boundary (P_{B_cri}). This implies the existence of an inherent non-ZVS gap between P_{A_cri} and P_{B_cri}, as shown in Fig. 2. Notably, when the voltage ratio

Received 12 October 2024; revised 30 November 2024; accepted 17 December 2024. Date of publication 25 December 2024; date of current version 28 January 2025. *(Corresponding author: Haifeng Lu.)*

Zhihua Fan, Jianyun Chai, and Xudong Sun are with the Department of Electrical Engineering, Tsinghua University, Beijing 100084, China (e-mail: fzh19@mails.tsinghua.edu.cn; chaijy@mail.tsinghua.edu.cn).

Haifeng Lu is with the Department of Electrical Engineering, Tsinghua University, Beijing 100084, China, and also with the School of Electrical Engineering, Xinjiang University, Urumqi 830047, China (e-mail: luhaifeng@mail.tsinghua.edu.cn).

Color versions of one or more figures in this article are available at https://doi.org/10.1109/TPEL.2024.3522328.

Digital Object Identifier 10.1109/TPEL.2024.3522328

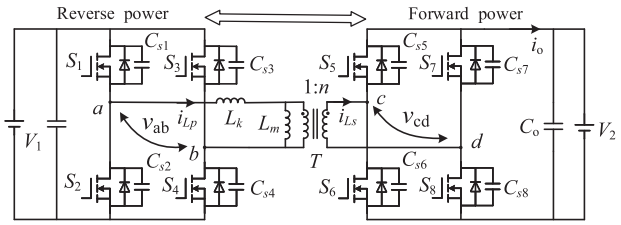

Fig. 1. Circuit diagram of the DAB converter.

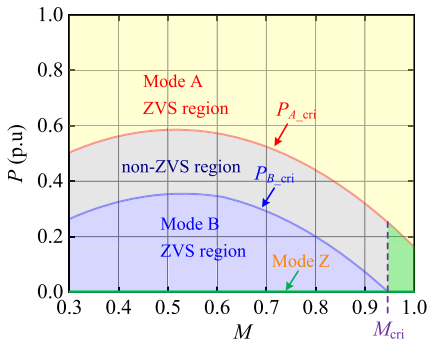

Fig. 2. ZVS region considering junction capacitance under traditional phase-shift control [9].

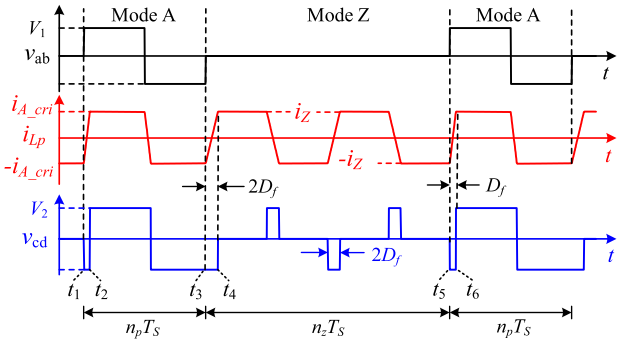

Fig. 3. QPPC waveforms at $M = 1$.

approaches unity gain ($M_{\text{cri}} \le M \le 1$), the ZVS region in mode B shrinks to disappear, while mode A also fails to achieve ZVS at the light load. To address the issues mentioned above, this letter discards mode B and takes the ZVS region of mode A ($P > P_{A\_\text{cri}}$) as power periods. Meanwhile, mode Z is constructed to achieve ZVS in a wide voltage gain range, including values near 1, and is utilized as nonpower periods. By alternating between the two ZVS-enabled modes, ZVS can be achieved based on the weighted average power of the two modes, which can effectively fill the inherent non-ZVS region.

A. Quantum Power Pulse Combination Modulation

Fig. 3 illustrates the operating waveforms of QPPC at $M = 1$, which consists of a sequence of integer power pulses ($n_p = 1$) or nonpower pulses ($n_z = 2$) with an integer period. During the power periods ($t_1 - t_3$), the DAB operates within the ZVS region of mode A. During nonpower periods ($t_4 - t_5$), the operating mode is referred to as mode Z, the primary bridge generates a voltage v_{ab} of 0 V, whereas the secondary bridge is actively controlled by a small duty cycle, allowing the phase-shift inductor to function as an adjustable magnetizing inductance. Hence, a controllable reactive current circulates between the two bridges, enabling ZVS operation in mode Z. Additionally, it allows switches to perform ZVS at the beginning of power periods and supports seamless transitions between the two modes. In mode Z, it is evident that only reactive current flows through the bridges without transferring active power. This allows the DAB to operate in intermittent CCM. It is worth noting that, when power flows in the reverse direction, the roles of the primary and secondary bridge are swapped.

The QPPC modulation involves the following key points: 1) ensuring ZVS at each commutating time ($t_1 \sim t_6$); 2) achieving seamless switching between the two modes without dc bias and extra transition intervals; 3) minimizing the reactive current i_Z in mode Z to reduce conduction loss.

According to [1], the critical ZVS current $i_{P\_A\_\text{cri}}$, $i_{S\_A\_\text{cri}}$ in mode A, and i_{Z_cri} in mode Z can be calculated as

$$\begin{cases} i_{Lp}(t_1) > i_{P\_A\_\text{cri}} = \sqrt{2Q_P \cdot (V_1 + V_2/n)/L} \\ i_{Lp}(t_2) > i_{S\_A\_\text{cri}} = \sqrt{2Q_S \cdot (V_1 + V_2/n)/L} \\ i_{Lp}(t_3) > i_{P\_A\_\text{cri}} = \sqrt{2Q_P \cdot (V_2/n)/L} \\ i_{Lp}(t_4) > i_{Z\_\text{cri}} = \sqrt{2Q_S \cdot (V_2/n)/L} \end{cases} \tag{1}$$

where Q_P and Q_S denote the stored charges of the junction capacitance in the primary and secondary sides, respectively.

When the DAB operates in mode A at $M = 1$, $i_{Lp}(t_1) = i_{Lp}(t_2)$ can be obtained. To achieve ZVS of all switches in mode A, the following relation should be met:

$$i_{Lp}(t_1) \ge i_{A\_\text{cri}} = \max(i_{P\_A\_\text{cri}}, i_{S\_A\_\text{cri}}). \tag{2}$$

The ZVS condition for mode Z requires $i_Z > i_{Z\_\text{cri}}$. Besides, when switching from mode Z to mode A, the ZVS condition at t_5 is $i_Z > i_{Z\_\text{cri}}$. Therefore, to minimize conduction losses while ensuring ZVS, $i_Z = \max(i_{A\_\text{cri}}, i_{Z\_\text{cri}})$ is set. According to (1), $i_{A\_\text{cri}} > i_{Z\_\text{cri}}$ can be obtained. Thus, the equation $i_Z = i_{A\_\text{cri}}$ can be got.

To eliminate dc bias during the dynamic transition, when switching from mode A to mode Z, the phase-shift angle is intentionally changed from D_f to $2D_f$, so that $i_{Lp}(t_3) = i_{Lp}(t_4) = i_{A\_\text{cri}}$, which also indicates that the duty cycle for mode Z is $2D_f$. D_f can be easily derived as

$$D_f = i_{A\_\text{cri\_pu}}. \tag{3}$$

The out power $P_{A\_\text{cri\_pu}}$ can be given as

$$P_{A\_\text{cri\_pu}} = -4i_{A\_\text{cri\_pu}}^2 + 4i_{A\_\text{cri\_pu}}. \tag{4}$$

Meanwhile, the base values of voltage, current, and power are defined as

$$\begin{cases} V_b = V_1 \\ I_b = V_b/(4f_sL) \\ P_b = V_1V_2/(8nf_sL) \end{cases}. \tag{5}$$

More generally, the QPPC waveforms at $M < 1$ is shown in Fig. 4. Considering the ZVS conditions at t_5 and t_6, i_Z must be greater than both $i_{P\_A\_\text{cri}}$ and $i_{S\_A\_\text{cri}}$. Therefore, $i_Z = i_{A\_\text{cri}}$ is set. D_Δ regulates the difference between $i_{Lp}(t_3)$ and i_Z, enabling seamless transitions between mode A and mode Z.

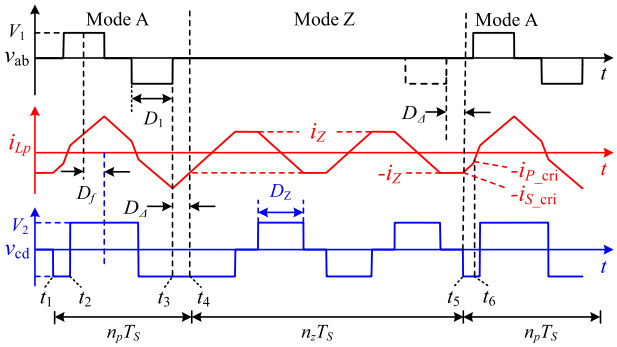

Fig. 4. QPPC waveforms at $M < 1$.

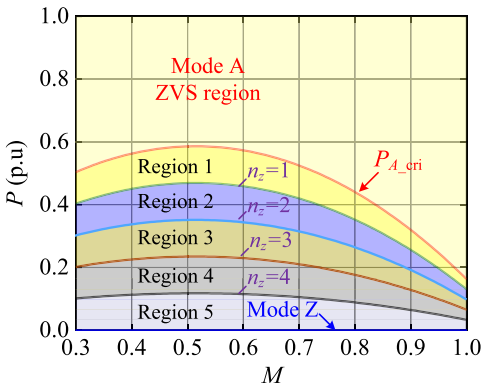

Fig. 5. ZVS region distribution with $n = 5$ under QPPC modulation.

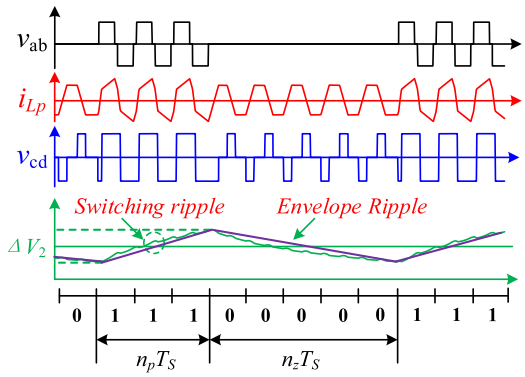

Fig. 6. Output voltage ripple for a continuous sequence {11100000}.

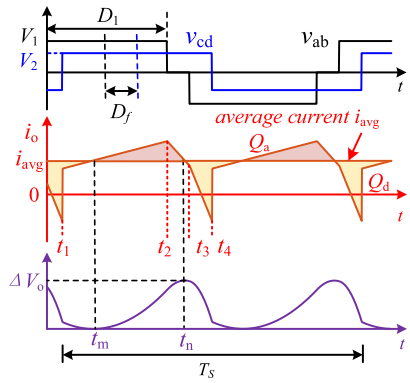

Fig. 7. Waveforms of i_o and its average value.

The expressions of D_1, D_f, D_Δ, and D_Z are calculated as

$$\begin{cases} D_Z = 2i_{Z\_pu}/M \\ D_f = (i_{S\_cri\_pu} + 1 - M)/2 \\ D_1 = (2M - 2MD_f - i_{P\_cri\_pu})/(1+M) \\ D_\Delta = D_1 - MD_1 + 2MD_f - i_{Z\_pu}. \end{cases} \tag{6}$$

The output power $P_{A\_cri\_pu}$ can be calculated as

$$P_{A\_cri\_pu} = -4D_f^2 - D_1^2 + 4D_f + 2D_1 - 1. \tag{7}$$

Assuming that the macroscopic period n consists of n_p periods in mode A and n_z periods in mode Z, As mode Z does not transfer active power, the weighted average power P_{ave} is expressed as

$$P_{\text{ave}} = P_{A\_cri} \cdot n_p/n. \tag{8}$$

The ZVS region distribution with $n = 5$ under QPPC modulation is shown in Fig. 5. When the load power falls below P_{A_cri}, ZVS can be achieved based on the weighted average power of mode A and mode Z. As a result, the power range below P_{A_cri} can be divided into n ZVS regions by average power curves, effectively covering the original non-ZVS regions.

B. Output Voltage Ripple

Let i denote the operating mode at the kth period ($i = 1$ for mode A, 0 for mode Z). The theoretical calculation of output voltage ripple is illustrated using a continuous sequence {11100000} as an example, and the output voltage ripple is depicted in Fig. 6. The output voltage ripple consists of two parts: switching ripple and envelope ripple. The switching ripple results from the harmonics component of the rectified current i_o and has a ripple frequency twice that of the switching frequency. The switching ripple is caused by the difference between i_o and its average value. The waveforms of i_o and its average are shown in Fig. 7. The shaded areas Q_a and Q_d represent the charges causing the upward and downward ripples of the output voltage, respectively.

By performing piecewise integration, the average current can be calculated as

$$i_{ave} = \int_{t_1}^{t_4} i_o(t)dt = \left(-4D_f^2 - D_1^2 + 4D_f + 2D_1 - 1\right)/2. \tag{9}$$

Considering only the case where $t_1 < t_m < t_n < t_3$, Q_a can be derived as

$$Q_a = \int_{t_m}^{t_n} (i_o(t) - i_{avg}) = \frac{(i_o(t_2) - i_{\text{ave}})^2}{8(M - M^2)} \tag{10}$$

Q_a for other cases can be calculated in a similar manner. The switching ripple can be calculated as

$$\Delta V_{os} = \frac{Q_a}{C_o}. \tag{11}$$

The above switching ripple calculation corresponds to the output voltage ripple of mode A under TPS control, and can

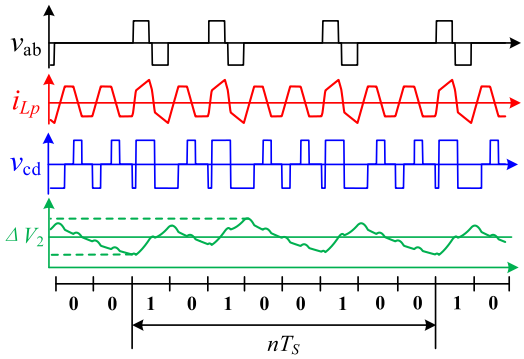

Fig. 8. Output voltage ripple waveforms for a sequence {10100100}.

be generalized to calculate the output voltage ripple for other modes.

The envelope ripple is induced by different operating modes. During power periods, the output capacitor charges, causing the output voltage to rise. Conversely, during nonpower periods, the output capacitor discharges into the load, causing the output voltage to fall. Assuming that a constant load current I_L discharges the output dc capacitor C_o during nonpower periods. The peak-to-peak value of envelope ripple ΔV_{oe} for a continuous sequence can be calculated as

$$\Delta V_{oe} = I_L \cdot n_z \cdot T_S / C_o. \tag{12}$$

Substituting $I_L = P_{\text{ave}}/V_2$ into (12), ΔV_{oe} is reformulated as

$$\Delta V_{oe} = \frac{n_z T_S P_{\text{ave}}}{C_o V_2} = \frac{T_S P_{A\_\text{cri}}}{C_o V_2} \cdot \frac{n_z n_p}{n_p + n_z}. \tag{13}$$

Assuming that macroscopic periods $n = 8$ consist of $n_p = 3$ and $n_z = 5$, various sequence combinations can be formed, such as {11100000} and {10100100}, each resulting in varying degrees of envelope ripple. The envelope ripple is shown in Fig. 8 for the sequence {10100100}. As seen, the envelope ripple for {10100100} is determined by the leading sequence {101} and can be calculated as

$$\Delta V_{oe} = \frac{(2\,(P_{A\_\text{cri}} - P_{\text{ave}}) - P_{\text{ave}}) \cdot T_S}{C_o V_2} = \frac{7 P_{A\_\text{cri}} T_S}{8 C_o V_2}. \tag{14}$$

The switching ripple and envelope ripple are independent of each other. The total output voltage ripple can be calculated by summing the two components. Given that $Q_a \ll I_L \cdot T_S$, the switching ripple is negligible compared to the envelope ripple. Consequently, the output voltage ripple is primarily determined by the envelope ripple.

The output voltage ripple calculation described above can be extended to other sequences. The voltage ripples for continuous sequences and optimum sequences are listed in Table I. It is found that the optimum sequence that minimizes voltage ripple is obtained when the power periods are most evenly distributed.

An alternative approach to reducing output voltage ripple is to increase the switching frequency of mode A, thereby lowering the critical ZVS power boundary P_{A_cri}. Fig. 9 shows P_{A_cri} varying with switching frequency ratio F. P_{A_cri} decreases as F increases. Based on (13), reducing P_{A_cri} can effectively lower ΔV_{oe}. However, beyond a certain frequency threshold, higher frequency introduces greater turn-OFF and conduction losses,

TABLE I
OUTPUT VOLTAGE RIPPLE FOR
$T_S = 10us, V_2 = 300V, C_{dc} = 4.7\mu F, P_{A\_\text{CRI}} = 320\,W$

		Continuous sequence		Optimum Sequence	
n	n_p	Sequence	Ripple(%)	Sequence	Ripple(%)
5	1	10000	0.61	10000	0.61
	2	11000	0.91	10100	0.30
	3	11100	0.91	11010	0.30
	4	11110	0.61	11110	0.61
6	1	100000	0.63	100000	0.63
	2	110000	1.01	100100	0.25
	3	111000	1.13	101010	0.13
	4	111100	1.01	110110	0.25
	5	111110	0.63	111110	0.63

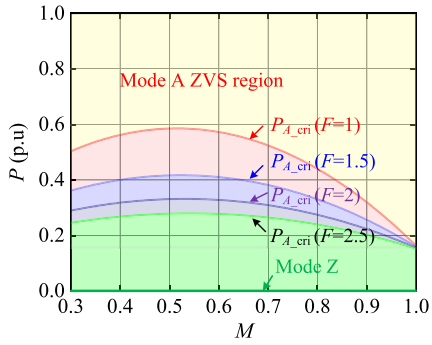

Fig. 9. P_{A_cri} varying with switching frequency ratio F.

TABLE II
EXPERIMENTAL PARAMETERS OF PROTOTYPE

Parameter	Value	Parameter	Value
V_1	40 V	$1:n$	1:7.5
V_2	150–300V	L	2.3 uH
f_s	100 kHz	L_m	35.6 uH
C_o	10 uF	Maximum P_o	1200 W
$S_1 - S_4$	LSGT10R018HC	$S_5 - S_8$	IPA65R400CE
$R_{ds(on)}$ of S_1	1.85mΩ	$R_{ds(on)}$ of S_5	400mΩ
C_{oss} of S_1	1984 pF	C_{oss} of S_5	41 pF
Transformer core	ECI51	Inductor core	PQI3525
Core material	DMR95	Core material	PC44

offsetting the benefits of ZVS [9]. Consequently, F should not be set excessively high. In this letter, a fixed frequency of $F = 1$ is selected to validate the effectiveness of the QPPC modulation.

C. Theoretical Loss Analysis

A DAB prototype was fabricated with specifications listed in Table II. By using the loss calculation method [10], this section performs a loss breakdown comparison with $M = 1$ at a load power of 160 W ($P_{A\_\text{cri}} = 320\,\text{W}, n_p = n_z = 2$). The analysis results are illustrated in Fig. 10. Based on the operating waveforms, the power loss of QPPC can be approximated as the weighted average loss of mode A and mode Z. Therefore, the power loss is linearized as: $n_p P_{A\_\text{loss}} + n_z P_{Z\_\text{loss}}$, where the loss P_{Z_loss} in mode Z remains low (about 5 W) due to ZVS operation, minimal transformer core loss caused by low peak-to-peak flux density, the inactive state of one bridge switches and the small turn-OFF current of another bridge switches. For mode A, when the load power equals P_{A_cri}, the loss P_{A_loss} can be estimated at

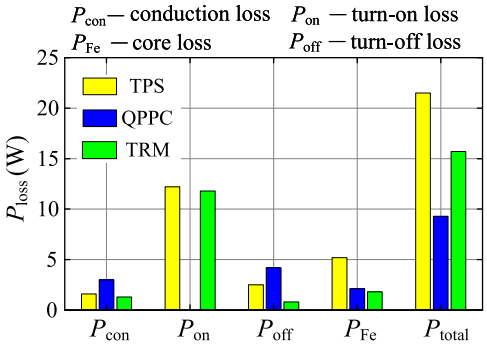

Fig. 10. Loss breakdown comparison at $M = 1$ (160 W).

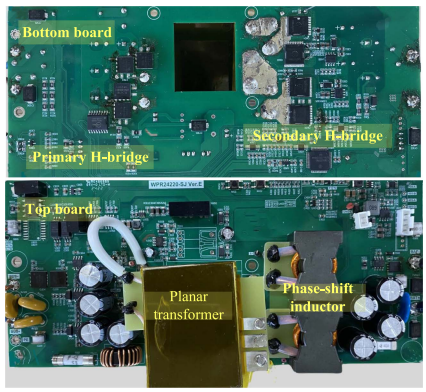

Fig. 11. Experimental prototype of the DAB converter.

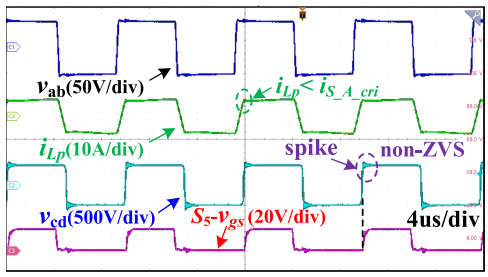

Fig. 12. Non-ZVS waveforms of mode A under TPS when $M = 1$.

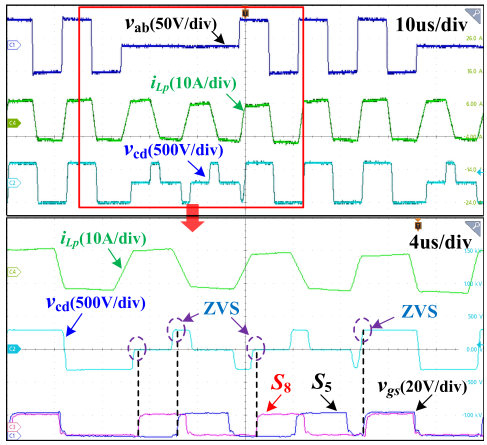

Fig. 13. ZVS waveforms of QPPC ($n_p = 3, n_z = 2$) when $M = 1$.

13.2 W, which is also relatively low. Therefore, the losses under QPPC can be minimized, as they correspond to the weighted average loss of the two modes.

As seen in Fig. 10, the total power loss under TPS [2] is considerably larger than that under QPPC, primarily due to the greater turn-ON loss caused by non-ZVS and the large transformer core loss. Similarly, due to its operation in DCM, TRM suffers from non-ZVS, resulting in higher power loss than QPPC. On the other hand, the conduction loss and turn-OFF loss under QPPC are relatively higher than TPS and TRM due to the larger reactive current in mode Z. Consequently, ZVS can reduce the switching loss significantly and thus improve the efficiency.

III. Experimental Results

To validate the effectiveness of the proposed method, An experimental prototype of a DAB converter was constructed as shown in Fig. 11, with its corresponding experimental parameters detailed in Table II.

A. ZVS Comparison Between TPS and QPPC at $M = 1$

Fig. 12 shows the experimental waveforms of mode A at $M = 1$ under TPS. When the output power $P_o = 190$ W is less than the critical ZVS power boundary $P_{A\_cri} = 320$ W, the turn-ON current of the secondary switches is lower than I_{A_cri}. This brings a voltage spike in v_{cd}, indicating that the DAB operates within the inherent non-ZVS region.

Fig. 13 illustrates the waveforms of QPPC ($n_p = 3, n_z = 2$) at $M = 1$. For comparison purposes, the average power under QPPC modulation ($P_{avg} = 3P_{A\_cri}/5 = 192$ W) is aligned with the output power under TPS to ensure consistency. As seen, the gate signals v_{gs} of switches S_5 and S_8 are given, and their drain-source voltages v_{ds} can be indirectly obtained from v_{cd}. Before S_5 and S_8 are turned ON, their junction capacitances have been discharged to 0 V, indicating that ZVS is achieved. Moreover, no voltage spike or ringing occurs in v_{ab} and v_{cd}, confirming ZVS operation. As seen from Fig. 13, the QPPC modulation ensures ZVS for both mode A and mode Z, as well as during dynamic processes, while preventing dc offset in the inductor current. Furthermore, by adjusting the number of power and nonpower periods within the macroscopic period, the average output power under QPPC can be regulated. Therefore, the QPPC modulation can achieve ZVS at power levels below P_{A_cri}, completely eliminating the inherent non-ZVS region.

B. ZVS Comparison Under Different Modulations at $M < 1$

Fig. 14(a) shows the non-ZVS waveforms of mode A under TPS at $M = 0.5$. When the output power P_o decreases from $P_{A\_cri} = 240$ W to 145 W, $\phi = D_f - (1 - D_1)/2$ gradually approaches zero, making it difficult to achieve ZVS. As seen from Fig. 14(a), the v_{ds} of the primary switches does not fully reach zero during the dead time, a condition referred to as partial ZVS. Meanwhile, a voltage spike is observed in the v_{cd}, indicating that the secondary switches lose ZVS. When P_o

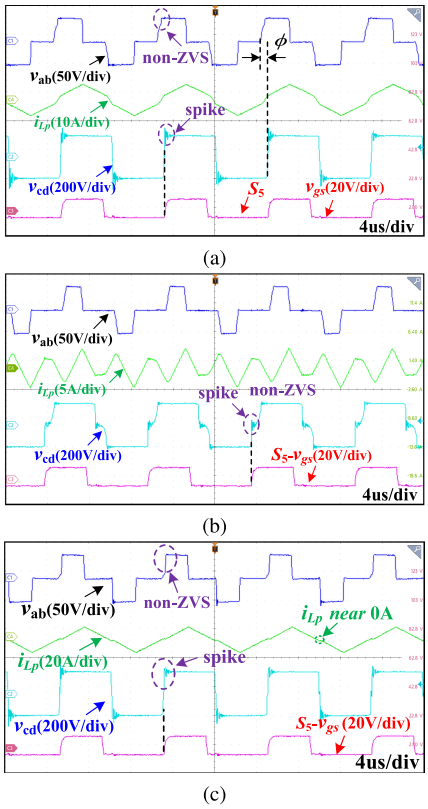

Fig. 14. Non-ZVS waveforms at $M = 0.5$. (a) Mode A of TPS. (b) Mode C of TPS in [1]. (c) TRM.

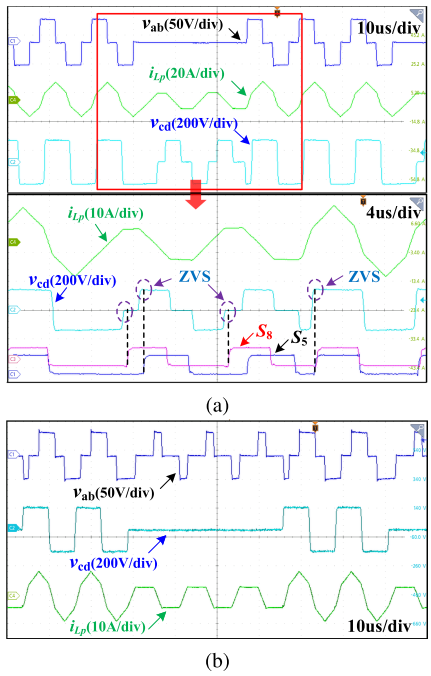

Fig. 15. ZVS waveforms of QPPC at $M = 0.5$. (a) Forward power ($n_p = 3, n_z = 2$). (b) Reverse power ($n_p = 2, n_z = 3$).

further decreases to 90 W, the DAB converter enters mode C under TPS control in [1], as shown in Fig. 14(b). In this case, the secondary switches are unable to achieve ZVS, implying that the DAB operates within the non-ZVS gap depicted in Fig. 2. Fig. 14(c) shows the non-ZVS waveforms under TRM (110 W). As seen, the inductor current takes on a triangular waveform, enabling ZCS of the switches. However, this compromises ZVS.

Fig. 15(a) illustrates the ZVS waveforms of QPPC ($n_p = 3, n_z = 2$) at $M = 0.5$ under forward power flow ($P_o = 145$ W). As seen, before the v_{gs} signals of S_5 and S_8 change from zero to positive, v_{ds} have already reached zero, so ZVS of S_5 and S_8 can be obtained. Moreover, no voltage spike or partial ZVS occurs in v_{ab} and v_{cd}, indicating that all switches can achieve ZVS. Besides, it should be noted that i_Z is maintained at the minimum level required for ZVS, which helps minimize conduction losses.

Fig. 15(b) shows the experimental waveforms of QPPC ($n_p = 2, n_z = 3$) under reverse power flow (96 W). The difference between forward and reverse power lies in the regulation of the inductor current in Mode Z. For forward power flow, it is regulated by the secondary bridge, whereas for reverse power flow, it is regulated by the primary bridge.

C. Output Voltage Ripple

To validate the theoretical calculations of output voltage ripple, the experimental waveforms at $M = 1$ under TPS, QPPC using the continuous sequence {11100} and QPPC using the optimum sequence {11010} are shows in Fig. 16. Substituting the experimental conditions of $P_{A\_cri} = 320$ W, $C_o = 10$ uF, $V_2 = 300$ V to the calculation formula in Section II yields $\Delta V_o = 0.16\,\text{V}, 1.28\,\text{V}, 0.85\,\text{V}$. The theoretical values are generally consistent with the experimental results $\Delta V_o = 0.2\,\text{V}, 1.56\,\text{V}, 0.76\,\text{V}$.

Fig. 17 shows the experimental waveforms at $M = 0.5$ for three different cases:TPS, QPPC with the sequence {11100000}, QPPC with the sequence {10100100}. The experimental conditions is $P_{A\_cri} = 240$ W, $C_o = 10$ uF, $V_2 = 150$ V. The theoretical values $\Delta V_o = 0.32\,\text{V}, 3.0\,\text{V}, 1.4\,\text{V}$ are nearly identical to the experimental values $\Delta V_o = 0.18\,\text{V}, 2.04\,\text{V}, 1.02\,\text{V}$.

D. Transient Waveforms

Fig. 18 shows the transient waveforms of power reversal from 106 to −320 W. Note that no dc bias or oscillation is observed in such a test. The entire test is completed within 50 us, demonstrating a fast transient response.

E. Loss and Efficiency

Fig. 19(a) and (b) plots loss curves and efficiency curves, respectively. For load power levels above 320 W, mode A under TPS is applied in all cases. At load power levels below 320 W, the DAB under TPS [2] suffers from partial ZVS, which increases the switching loss, thereby leading to lower efficiency. The loss curves of TRM and QPPC in intermittent operation exhibit distinct linearized trends. The experimental results indicate that QPPC has lower power losses than TRM, due to the significant reduction in switching losses enabled by ZVS. However, the QPPC may lead to increased conduction losses caused by the reactive current flowing in mode Z. Thus, within the extreme

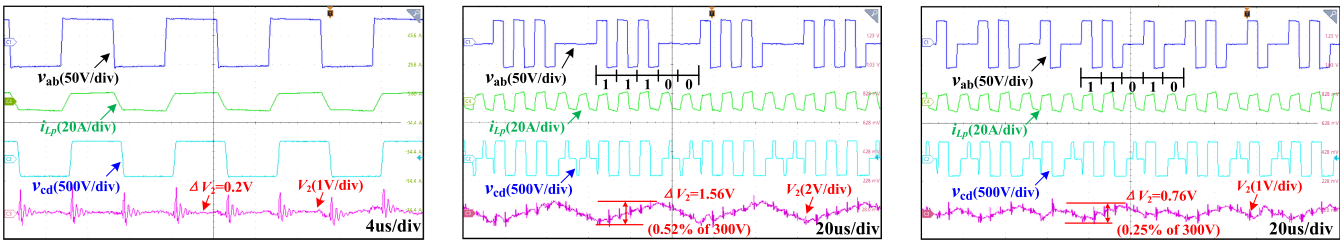

(a) (b) (c)

Fig. 16. Output voltage ripple at $M = 1$. (a) Mode A under TPS. (b) Continuous sequence {11100}. (c) Optimum sequence {11010}.

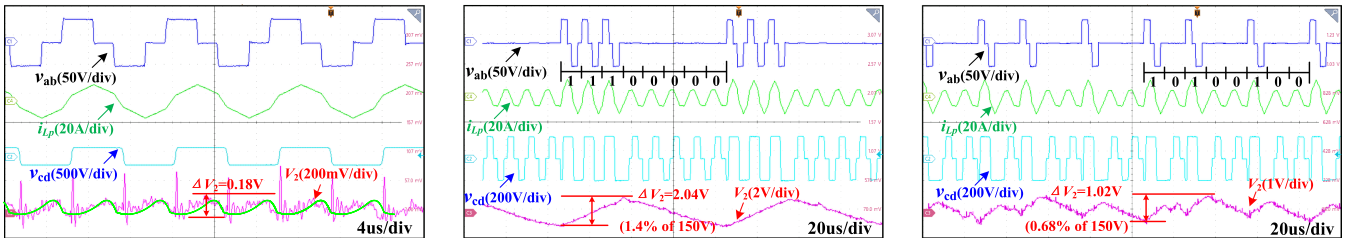

(a) (b) (c)

Fig. 17. Output voltage ripple at $M = 0.5$. (a) Mode a under TPS. (b) Continuous sequence {11100000}. (c) Optimum sequence {10100100}.

TABLE III
COMPARISONS OF DIFFERENT MODULATIONS

Items	TPS[2]	TRM[4]	TZM with magnetizing current[6]	QPPC
Soft switching	Non-ZVS gap	ZCS for four switches	ZVS in full load rang	ZVS in full load rang
RMS current	Small	Smallest	Large	Small
Peak current	Medium	Smallest	Large	Small (average)
Switching frequency	Fixed frequency	Fixed frequency	Fixed frequency	Small (average)
Transformer core loss	Large when M near 1	Small	Small	Small (average)
Control complexity	Small	Small	Medium	Large

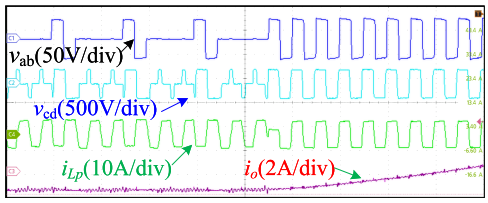

Fig. 18. Transient waveforms when power reversal.

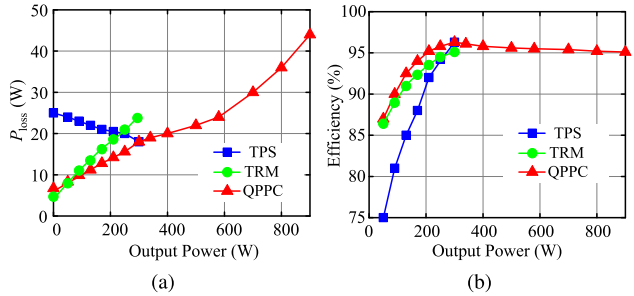

(a) (b)

Fig. 19. $M = 1$ (a) Loss versus output power. (b) Efficiency curve.

light load ranges (about 30 W), the TRM has higher efficiency than QPPC.

The QPPC is compared with other methods in various aspects, as summarized in Table III.

IV. CONCLUSION

This letter proposes the QPPC modulation, which alternates between power pulses in mode A and nonpower pulses in mode Z. The mode Z is constructed to make the inductor current controllable, not only enabling ZVS in a wide voltage gain range but also ensuring seamless switching between the two modes. The load power can be approximated by the average power of QPPC. Therefore, the full load range ZVS is achieved in terms of average power. This method is straightforward to implement and does not require any additional hardware resources. Experimental results show that the method significantly improves overall efficiency.

However, this method may increase the output capacitor voltage ripple, which can be mitigated by adjusting the sequence of power and nonpower periods.

REFERENCES

[1] Z. Wang, C. Li, J. Liu, and Z. Zheng, "Influence of junction-capacitance and dead-time on dual-active-bridge actual soft-switching-range: Analytic analysis and solution," *IEEE Trans. Power Electron.*, vol. 38, no. 5, pp. 6157–6168, May 2023.

[2] A. K. Bhattacharjee and I. Batarseh, "Optimum hybrid modulation for improvement of efficiency over wide operating range for triple-phase-shift dual-active-bridge converter," *IEEE Trans. Power Electron.*, vol. 35, no. 5, pp. 4804–4818, May 2020.

[3] A. Tong, L. Hang, G. Li, X. Jiang, and S. Gao, "Modeling and analysis of a dual-active-bridge-isolated bidirectional DC/DC converter to minimize RMS current with whole operating range," *IEEE Trans. Power Electron.*, vol. 33, no. 6, pp. 5302–5316, Jun. 2018.

[4] T. Hirose, M. Takasaki, and Y. Ishizuka, "A power efficiency improvement technique for a bidirectional dual active bridge DC–DC converter at light load," *IEEE Trans. Ind. Appl.*, vol. 50, no. 6, pp. 4047–4055, Nov./Dec. 2014.

[5] S. Zengin and M. Boztepe, "A novel current modulation method to eliminate low-frequency harmonics in single-stage dual active bridge AC–DC converter," *IEEE Trans. Ind. Electron.*, vol. 67, no. 2, pp. 1048–1058, Feb. 2020.

[6] G. Xu, D. Sha, and J. Zhang, "Unified boundary trapezoidal modulation control utilizing fixed duty cycle compensation and magnetizing current design for dual active bridge DC–DC converter," *IEEE Trans. Power Electron.*, vol. 32, no. 3, pp. 2243–2252, Mar. 2017.

[7] Z. Ye, C. Li, J. Liu, and Z. Zheng, "Towards full range zero-voltage switching of DAB converters: An improved multi-mode modulation at light loads under close-to-unity voltage ratio," *IEEE Trans. Power Electron.*, vol. 38, no. 6, pp. 6912–6917, Jun. 2023.

[8] R. Haneda and H. Akagi, "Design and performance of the 850-V 100-kW 16-kHz bidirectional isolated DC–DC converter using SiC-MOSFET/SBD H-bridge modules," *IEEE Trans. Power Electron.*, vol. 35, no. 10, pp. 10013–10025, Oct. 2020.

[9] Z. Fan, H. Lu, J. Chai, Y. Li, and X. Sun, "Partition variable frequency and EPS hybrid control to achieve full load range ZVS for dual active bridge converters," *IEEE J. Emerg. Sel. Topics Power Electron.*, vol. 12, no. 1, pp. 143–155, Feb. 2024.

[10] D. Sha, J. Zhang, and T. Sun, "Multimode control strategy for SiC Mosfets based semi-dual active bridge DC–DC converter," *IEEE Trans. Power Electron.*, vol. 34, no. 6, pp. 5476–5486, Jun. 2019.